Pharm Res (2015) 32:1368–1382
DOI 10.1007/s11095-014-1540-y

RESEARCH PAPER

Pulmonary Biodistribution and Cellular Uptake of Intranasally Administered Monodisperse Particles

Timothy M. Brenza • Latrisha K. Petersen • Yanjie Zhang • Lucas M. Huntimer • Amanda E. Ramer-Tait • Jesse M. Hostetter • Michael J. Wannemuehler • Balaji Narasimhan

Received: 28 May 2014 / Accepted: 1 October 2014 / Published online: 9 October 2014

ABSTRACT

Purpose For the rational design of nanovaccines against respiratory pathogens, careful selection of optimal particle size and chemistry is paramount. This work investigates the impact of these properties on the deposition, biodistribution, and cellular interactions of nanoparticles within the lungs.

Method In this work, biodegradable poly(sebacic anhydride) (poly(SA)) nanoparticles of multiple sizes were synthesized with narrow particle size distributions. The lung deposition and retention as well as the internalization by phagocytic cells of these particles were compared to that of non-degradable monodisperse polystyrene nanoparticles of similar sizes.

Results The initial deposition of intranasally administered particles in the lungs was dependent on primary particle size, with maximal deposition occurring for the 360–470 nm particles, regardless of chemistry. Over time, both particle size and chemistry affected the frequency of particle-positive cells and the specific cell types taking up particles. The biodegradable poly(SA) particles associated more closely with phagocytic cells and the dynamics of this association impacted the clearance of these particles from the lung.

Conclusions The findings reported herein indicate that both size and chemistry control the fate of intranasally administered particles and that the dynamics of particle association with phagocytic cells in the lungs provide important insights for the rational design of pulmonary vaccine delivery vehicles.

KEY WORDS polyanhydrides · nanoparticle · biodistribution · vaccines · pulmonary · histology

ABBREVIATIONS

APC	Antigen presenting cell
DC	Dendritic cell
H&E	Hematoxylin and eosin
MFI	Mean fluorescence intensity
MΦ	Macrophage
PMN	Polymorphonuclear leukocyte
poly(SA)	Poly(sebacic anhydride)
PS	Polystyrene

INTRODUCTION

Biodegradable nanoparticle-based systems possess favorable attributes for therapeutic drug delivery, vaccination, and biomedical imaging (1–3). In particular, polyanhydride particles have been utilized to provide sustained delivery of anesthetics, chemotherapeutics, insulin, analgesics, antibiotics, vaccine antigens, and proteins (4–10). Polyanhydride nanoparticles possess excellent biocompatibility and are typically characterized by surface erosion, both of which are central to their utilization as

Electronic supplementary material The online version of this article (doi:10.1007/s11095-014-1540-y) contains supplementary material, which is available to authorized users.

T. M. Brenza • L. K. Petersen • Y. Zhang • B. Narasimhan (✉)
Department of Chemical and Biological Engineering, Iowa State University, 2035 Sweeney Hall, Ames, Iowa 50011, USA
e-mail: nbalaji@iastate.edu

L. M. Huntimer • A. E. Ramer-Tait • M. J. Wannemuehler
Department of Veterinary Microbiology and Preventive Medicine, Iowa State University, Ames, IA, USA

J. M. Hostetter
Department of Veterinary Pathology, Iowa State University
Ames, IA, USA

drug and vaccine carriers (11). Size and route of administration have been shown to greatly impact the biodistribution and bioavailability of biodegradable particles (12–16).

For treatment of or immunization against respiratory infections, intranasal administration offers many advantages, including ease of administration, induction of systemic and mucosal immunity, and reduced systemic exposure (17). In this regard, size plays a critical role in the initial deposition of particles within the respiratory tract as evidenced by a significant decrease in the deposition of polydisperse aerosolized particles in the lungs of mice (from 10.7 for 500 nm (activity median aerodynamic diameter) particles to 2.2% for 1,000 nm particles) (14). This trend was also observed in experiments measuring drug concentration in the lung following the administration of nebulized suspensions of 200 nm and 1,600 nm fluticasone particles (16). In these experiments, the intranasal administration of the 200 nm particles resulted in measurable drug concentrations in lung tissue and plasma, while the resulting drug concentration following administration of the 1,600 nm particles was below the level of detection suggesting that the larger particles failed to be deposited in the lungs (16). However, there is currently a gap in the literature describing the relative deposition of intranasally administered particulate delivery vehicles designed for vaccination.

The design of efficacious vaccine formulations based on biodegradable nano-adjuvants is a complex function of several parameters including route of administration, antigen dose, sustained exposure of antigen, and immunomodulatory properties of the adjuvant (18). Particle size, shape, and chemistry have all been shown to influence particle uptake by antigen presenting cells (APCs), which is an essential first step in the induction of an adaptive immune response (19–21). Our previous work demonstrated the efficacy of a single intranasal administration of F1-V loaded polyanhydride nanoparticles co-delivered with soluble F1-V that provided 100% protection against a lethal challenge of *Yersinia pestis* (22,23). In that work, the lead candidate nanovaccine formulation contained antigen-encapsulated polydisperse particles with a mean diameter of 196 ± 77 nm, with sizes ranging from 80 to 600 nm. This suggests that there is sufficient penetration of the nanovaccine and cellular interaction to stimulate an immune response for particles within this size range. However, the interaction of specific sizes of these nanovaccines with cells *in vivo* and comparisons to other particulate chemistries have not been studied.

For the rational design of pulmonary nanovaccines and delivery systems, careful selection of particle size and chemistry is paramount because these properties influence the initial deposition, biodistribution, cellular interactions, and induction of immune responses. Previous work has utilized monodisperse non-degradable particles (e.g., polystyrene (PS) or inorganic particles) for size comparative studies (3,22,24,25); however, there are no studies detailing the pulmonary biodistribution or the cellular uptake of monodisperse biodegradable particles following intranasal administration. In this regard, the synthesis of monodisperse biodegradable particles is necessary to delineate the effect of particle size on pulmonary deposition and cellular uptake, which influence the induction of an antigen-specific immune response. In this work, we synthesized monodisperse biodegradable poly(sebacic anhydride) (poly(SA)) nanoparticles and compared their pulmonary biodistribution and cellular uptake with non-degradable monodisperse PS nanoparticles of similar sizes. Our results indicate that both particle size and chemistry affected the pulmonary biodistribution, cellular uptake, and the kinetics of particle retention in the lung. These results provide a foundation from which the differential effects of particle size and polymer chemistry on interactions with the respiratory immune system can be elucidated.

MATERIALS AND METHODS

Particle Synthesis and Characterization

Synthesis of poly(SA) was performed as described previously (26,27). Proton NMR (VXR-300, Varian) was used to measure molecular weight and polymer purity. For nanometer sized particles, rhodamine B (λ_{ex} = 554 nm, λ_{em} = 627 nm (Acidic EtOH)) (Sigma Aldrich, St. Louis, MO) was incorporated into the poly(SA) particles at 0.5 wt.% by a modified anti-solvent nano-encapsulation method (19). Briefly, the synthesized polymer (20 or 40 mg), rhodamine B dye (0.1 or 0.2 mg), and 50 μL Span 80 (Sigma Aldrich, St. Louis, MO) were dispersed in 1 mL of chloroform (Fisher Scientific, Pittsburgh, PA) and sonicated for 60 s with a sonication probe (Sonics and Materials, Newtown, CT). The solution was poured into 80 mL of hexanes (Fisher Scientific, Pittsburgh, PA) and the particles were recovered by centrifugation and dried in a vacuum chamber. Flash precipitation with the lower polymer concentration in the solvent resulted in a smaller final particle size. For the micron-sized particles, rhodamine B was incorporated into the poly(SA) particles at 1.0 wt.% by spray drying. The synthesized polymer (250 mg), rhodamine B dye (2.5 mg), and 15 μL span 80 were dispersed in 25 mL of methylene chloride (Fischer Scientific, Pittsburgh, PA) and sonicated for 60 s with a probe sonicator. The solution was loaded into a gas tight syringe and fed to a bench-top spray dryer (Buechi, Switzerland) at a rate of 3 mL/min. The spray dryer was operated with argon as the feed gas, at a feed temperature of 40°C, at a vacuum of −50 bar, with a high efficiency cyclone and solvent condenser. SPHERO™ fluorescent PS particles (λ_{ex} = 580 nm, λ_{em} = 620 nm (water)) (Spherotech, Lake Forest, IL) were purchased to be similar in size to the synthesized poly(SA) particles. The particle

morphology and primary particle size were determined using scanning electron microscopy (Quanta 250 FE-SEM) (FEI, Hillsboro, OR) for both poly(SA) and PS particles. ImageJ 1.43u software (National Institutes of Health, Bethesda, MD) was utilized to quantify primary particle sizes for construction of the particle size distribution.

Particle Administration

Six-week old female C57BL/6 mice were obtained from Harlan Laboratories (Indianapolis, IN) and maintained under specific pathogen-free conditions. All procedures involving animals adhered to the "Principles of Laboratory Animal Care" (NIH publication #85–23, revised in 1985) and were approved by The Institutional Committee on Animal Care and Use at Iowa State University. Prior to particle administration, mice were deeply anesthetized via intraperitoneal injection of a ketamine/xylazine cocktail. The particles were administered by pipetting 10–15 μL suspension into one nostril and allowing it to be inhaled. This process was repeated, alternating nostrils, until the mice were administered a total of 0.5 mg of particles suspended in 50 μL PBS. The administered dose of particles was consistent with previously published nanovaccine regimen to mice (22,23). The PBS was added to the dry particles immediately prior to administration and a single particle suspension was achieved using a Vibra-Cell™ sonicator (Sonics and Materials, Newtown, CT) at 40 W for 60 s. Mice were administered particles in groups based on particle size. Each group consisted of equal numbers of mice administered poly(SA) and PS particles, either 5 or 10 for each terminal time point. Additional (1–2) mice for each terminal time point were administered 50 μL PBS and were used as experimental controls within each group. Animals were euthanized by CO_2 asphyxiation at 6, 12, and 24 h post administration for the 250 nm particles and at 6, 12, 24, and 48 h for the larger sized particles.

Imaging Excised Tissue

The excised tissue for each mouse was analyzed for fluorescence using an *In Vivo* Multispectral FX Pro imaging system (Carestream, Rochester, NY). The lungs were arranged on the imaging tray with the left lobe to the left of the trachea and the right lobes (apical, azygous, cardiac, and diaphramic) spread out to the right of the trachea. The excised tissues were exposed for 5 min to light through an excitation filter of 550 nm and collected with an emission filter of 750 nm. ImageJ was used to process and quantify the images. A threshold was applied to the white light images of the tissue to establish the region of interest (ROI) outlining the tissues. The fluorescent image was inverted and background was subtracted using a 50.0 pixel rolling ball radius. The fluorescent intensity was then quantified for each ROI. Images were false colored using the lookup table "fire" and brightness and contrast parameters were set to a 250 minimum and 2,000 maximum intensity, after which the ROI outline was overlaid upon the fluorescent image. The fluorescence intensity was averaged over the ROI to determine quantitative values of mean fluorescence intensity (MFI) for the tissue. Background fluorescence intensity was established from images of saline administered mice, which were included in each imaging session as a control.

Histological Evaluation

The left lobe of the lung and trachea was fixed in 10% neutral buffered formalin. Tissues were paraffin embedded, sectioned, and stained with hematoxylin and eosin (H&E). Stained tissue sections were evaluated using an Olympus BX 40 microscope. Photomicrographs of tissue sections were acquired using an Olympus DP26 digital camera with Olympus Cell Sense software. Tissues were evaluated, blindly, by a board-certified veterinary pathologist (JM Hostetter) using a histopathological scoring system adapted from a similar study (28). Scores of 0–5 were assigned to five independent parameters: inflammatory infiltration, necrosis, edema, hemorrhage, and bronchus-associated lymphoid tissue hyperplasia. A score of zero indicated the parameter was absent and a score of five indicated that the parameter was diffuse and interrupted normal tissue architecture. For inflammatory infiltration, the type of cellular infiltrate and the anatomical locations were also noted.

Flow Cytometry

The right lung (apical, azygous, cardiac, and diaphramic lobes) without the trachea was prepared for flow cytometry using the following method. The tissue was incubated in calcium and magnesium free Hank's balanced salt solution (HBSS) with 1 mg/mL collagenase D for 20 min at 37°C. Single cell suspensions were prepared using a gentleMACS^{TM} dissociator (Miltenyi Biotec, Cambridge, MA). Debris was removed by passing the suspension through a 40 μm cell straining filter (BD Falcon, San Jose, CA) and red blood cells were lysed with ACK lysis buffer. Approximately 5×10^6 cells (determined by a BD Coulter Cell Counter) were first suspended in PBS supplemented with 0.1 mg/mL FBS, 10 μg/mL sodium azide, and 0.1 mg/mL rat IgG. The cell suspension was then stained for cell surface markers and incubated for 30 min at 4°C. The following fluorescently conjugated antibodies and respective isotypes were purchased from: eBioscience (San Diego, CA) for CD11c PerCP/Cy 5.5 (clone N418) and Armenian hamster IgG isotype (clone eBio299Arm), CD11b PE (clone M1/70) and rat IgG2b isotype (clone R2B-7C3) and CD324 AF488 (clone DECMA-1) and mouse IgG2a κ isotype (clone eBM2a);

BioLegend (San Diego, CA) for F4/80 APC/Cy7 (clone BM8) and rat IgG2a κ isotype (clone RTK2758); and BD Biosciences (San Diego, CA) for Ly6 C/G APC (clone RB6-8C5) and rat IgG2b κ isotype (clone A95-1). After staining, the lung homogenate was washed twice with PBS, supplemented with 0.1 mg/mL FBS and 10 μg/mL sodium azide, and then fixed with stabilizing fixative (BD Biosciences, San Jose, CA). The cell suspension was analyzed by flow cytometry (FACSCanto, BD Biosciences, San Jose, CA) using two excitation lasers (488 and 633 nm) configured for eight fluorescent parameters in addition to forward scatter (FSC) and side scatter (SSC). The complete contents of the tubes were analyzed by flow cytometry and an average of 92,000 events per sample were captured and evaluated. Flow cytometric data was analyzed using FlowJo v10 (Tree Star, Ashland, OR). Controls consisting of a single fluorophore and fluorescence minus one with isotype controls were used in the flow cytometric gating and data analysis. A background fluorescent cell population was established from saline administered mice that were included in each flow cytometry session as a control (Supplemental Figure 1 shows a representative example).

Statistics

GraphPad Prism version 6.01 (San Diego, CA) was used for figure preparation and statistical analysis. One sample T-tests were used to determine significant difference from baseline values with a p-value less of 0.05 or less. Two way ANOVA's using Tukey's multiple comparisons test with an alpha of 0.05 were used for comparisons across chemistry, time, and type of cell marker (Figs. 3, 4, 5 and Table III).

RESULTS

Particle Characterization

Proton NMR was used to determine the molecular weight of the synthesized poly(SA). The average molecular weight of poly(SA) varied from 10,000 to 18,000 Da, in agreement with previous work (29–32). Scanning electron photomicrographs of rhodamine B-loaded poly(SA) nanoparticles show the uniformity of the size and spherical morphology of the synthesized particles (Fig. 1a).

The geometric size distributions for the poly(SA) and the PS particles are shown in Fig. 1b and c, respectively (Table I). For this work, we have categorized particles with a geometric standard deviation (GSD) less than 1.2 as nominally monodisperse. In each case, the PS particles had a narrower size range than the poly(SA) particles, as indicated by the smaller GSD. The 2,500 nm poly(SA) particles had the highest polydispersity with a GSD of 1.55 (Table I).

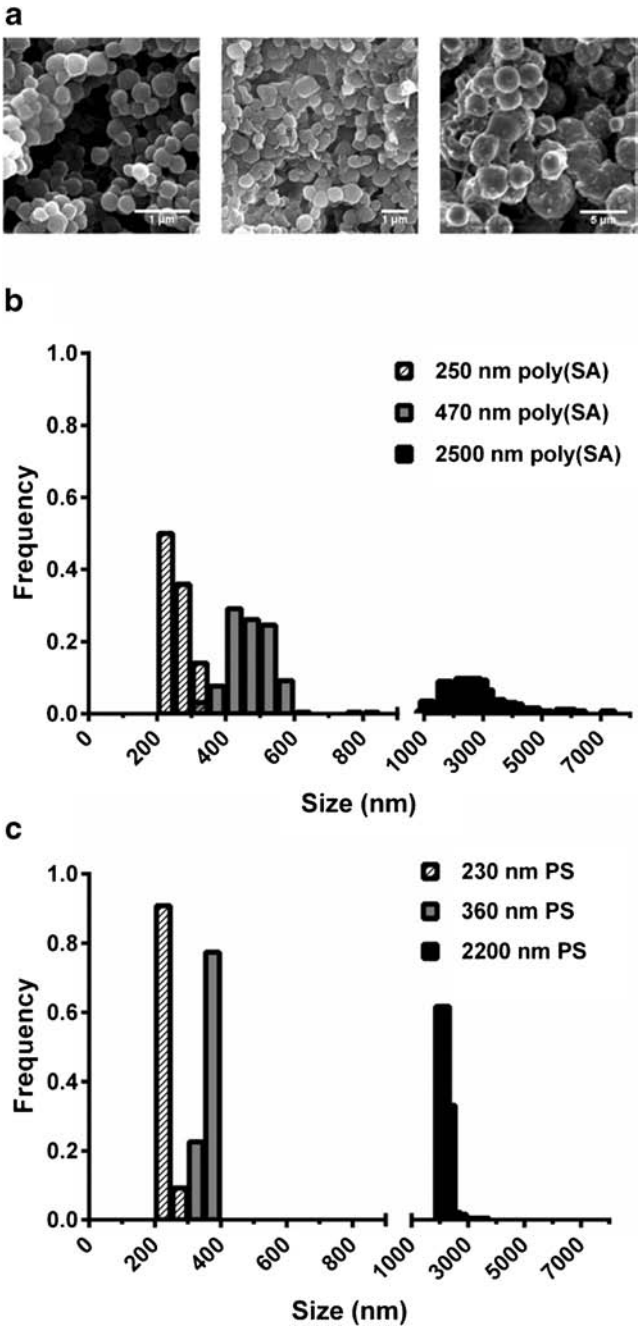

Fig. 1 Particle size distributions and morphology of synthesized poly(SA) and commercial PS particles. **a** Representative SEM images of rhodamine B-loaded poly(SA) particles showing spherical shape and uniformity of size. Images from left to right are of the 250, 470, and 2,500 nm particles. Particle size distribution is shown as the frequency of the total particle population of the **b** rhodamine B-loaded poly(SA) and **c** commercial PS particles falling in that size bin. Counts of particle size determined from SEM images ($n = 64$, 65, 256 for poly(SA) and 131, 195, 193 for PS).

Pulmonary Biodistribution and Clearance upon Intranasal Administration

The pulmonary biodistribution of the nanoparticles was monitored and representative examples of the mean fluorescence intensity (MFI) measured for the particles in the excised lungs

Table I Particle Size Distributions

Particle type	Diameter [nm][a]	Geometric SD	Polydispersity index (PDI)[b]
Poly(SA)	250	1.17	0.020
	470	1.15	0.017
	2,500	1.55[I]	0.187
PS	230	1.12	0.004
	360	1.09	0.003
	2,200	1.09[I]	0.006

[a] Diameter determined as the number geometric mean (CGM) of the particle population

[b] PDI calculated as $(SD)^2/(Mean)^2$

[I] Indicates statistically significant difference between chemistries ($p = 0.0002$)

of the mice are shown in Fig. 2 and quantified in Fig. 3. In these images, the greatest initial (i.e., 6 h post-administration) deposition of particles was observed in mice administered the 470 nm poly(SA) particles. Amounts similar to the 470 nm poly(SA) particles were observed in mice which received the 230 and 360 nm PS particles. In the groups with significant amounts of particle fluorescence, there was punctate fluorescent signal as opposed to diffuse fluorescence throughout the lung (Fig. 2). Over time, a decrease in the MFI of the 470 nm poly(SA) particles was observed between one and two days post-administration, which was not the case for the non-degradable PS particles.

The fluorescence intensity due to the biodegradable poly(SA) particles was significantly greater than the background (i.e., saline-treated) lung fluorescence at 24 h post-administration for the 250 nm and 2,500 nm sized particles (Fig. 3). While the lungs from the mice administered 470 nm poly(SA) particles remained consistent in intensity over the first 24 h, only the MFI at 6 and 12 h post-administration were

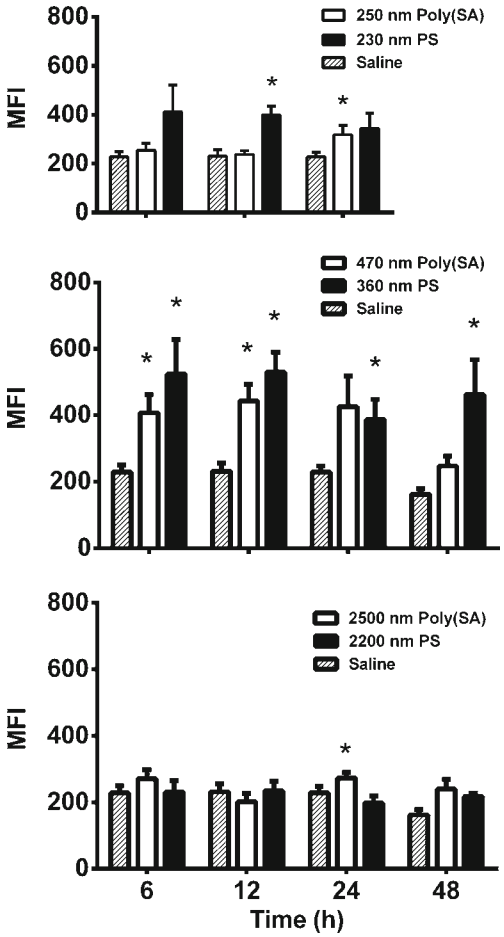

Fig. 3 The presence of the administered particles within the respiratory tract was estimated based on the mean fluorescence intensity (MFI) as shown in Fig. 2. The region of interest (ROI) was defined for each excised lung and the data is presented as the mean ± standard error. The *asterisk* (*) indicates statistical significance compared to lungs from mice that were administered saline ($p < 0.05$). Each treatment group at each time point consisted of a total of 10 mice.

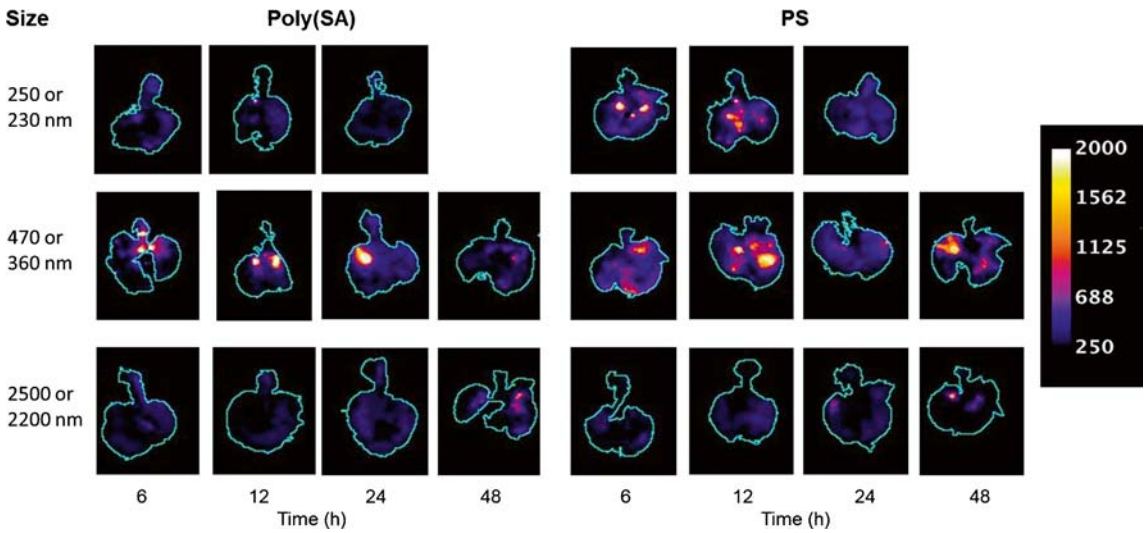

Fig. 2 Representative images of the respiratory tract showing mean fluorescence intensity associated with the pulmonary deposition of the indicated sizes of poly(SA) and PS particles over 48 h. The intensity scale is depicted on the right side of the image. The cyan outline of excised lung was generated using the light image of the lung as a guide and represents the region of interest (ROI) from which the relative fluorescence intensity was obtained for each excised lung.

significantly different than that of saline-treated mice (Fig. 3). Similarly, the MFI of the lungs excised from the mice that received the 230 nm PS particles ranged from 440 to 310 over the first 24 h, but only the MFI at 12 h post-administration was significantly different than background. The MFI of the lungs from mice administered the 360 nm PS particles was significantly greater than background for all time points measured, while that of the 2,200 nm PS particles was similar to background for all times. The only dynamic differences in deposition were observed for the lungs recovered from mice administered the 250 nm poly(SA) particles as evidenced by the increased MFI between 12 and 24 h, and for mice given the 470 nm poly(SA) particles in that the MFI decreased between 24 and 48 h post-administration. This indicates that non-degradable PS nanoparticles that deposited within the respiratory tract, regardless of size, were retained within the lung for the duration of the experiment. On the other hand, the MFI resulting from the biodegradable poly(SA) particles exhibited dynamic changes that suggest differential deposition, erosion, or clearance from the lung based on the size of the nanoparticles following intranasal administration.

Histological Evaluation of Lung Tissue

Tissue sections of mouse lung were stained with H&E and evaluated in a blinded study by a board-certified veterinary pathologist. Representative images of H&E stained lung sections are presented in Fig. 4a. Of the 12 tissue samples evaluated from mice that were administered saline, two received a score of one and two received a score of two for inflammatory infiltration and one received a score of one for bronchial associated lymphoid tissue (BALT) hyperplasia. All the lung tissue sections from the mice administered saline were scored as zero for necrosis, edema, and hemorrhage, indicating the absence of these parameters.

Inflammatory infiltration was the most prevalent parameter identified (73% of all particle administered mice) and the inflammatory infiltration scores are shown in Fig. 4b for the different particle sizes and types over time. For all but the 2,200 nm PS particles, a trend was observed where the inflammatory infiltration increased between 6 and 24 h post-administration but did not reach statistical significance due to the high variability in the scoring of the 24 h time point for that group. The lungs of the mice administered the 360 nm PS, 470 nm poly(SA), and 2,500 nm poly(SA) particles all showed a decrease in the inflammatory infiltration score between 24 and 48 h. Based on the scoring scale, only the mice which received 360 nm PS particles (over the entire 48 h) and the 2,200 nm PS particles (at 6 h) showed inflammatory infiltration in the lung tissue that was statistically greater than that observed in saline administered mice.

Neutrophils were the primary cell type in the inflammatory infiltration and were recruited into the lung following administration of all particles, regardless of chemistry, size or time point post administration. Plasma cells (based on cell staining and nucleus evaluation) were only observed in the infiltrate at 6 h post-administration for the 250 nm and 470 nm poly(SA) particle treated mice. Macrophages were observed in the inflammatory infiltration at 6 h post administration for the 2,500 nm poly(SA) and 2,200 nm PS particle treated mice. Macrophages were also present in the inflammatory infiltration at 24 h post-administration for all the poly(SA) particle treated mice, but only the 230 nm PS particle treated mice. At 48 h post-administration macrophages were present in the cellular infiltrate induced by the 470 nm and 2,500 nm poly(SA) as well as the 360 nm and 2,200 nm PS particle treated mice. Anatomically, the inflammatory infiltration was predominantly located within the alveolar, bronchiolar, and peribronchiolar spaces. Inflammatory infiltration was also observed to a lesser extent in perivascular spaces (21% of mice with an inflammatory infiltration score above zero).

Edema, hemorrhage and BALT hyperplasia were not frequently observed and were mild when observed (scores of 1–2). Necrosis was more prevalent (within 41% of mice administered particles) but closely tracked with the presence of an inflammatory infiltration in both occurrence and intensity. Necrosis is likely due to neutrophil-mediated pulmonary damage. The combined histological scores for all five parameters are presented by particle size, chemistry and time in Supplemental Figure 1.

Particle-Cell Association

Population of cells associated with particles

Flow cytometry was utilized to quantify the kinetics of nanoparticle association with different cellular populations. Viable cells that were associated (i.e., internalized or surface bound) with particles were gated and quantified (Supplemental Figure 2, Table II, and Fig. 5). The percentage of viable cells associated with particles at 6 h post-administration was low (3–5%).

For lung homogenates prepared from mice that were administered poly(SA) particles, the percentage of cells associated with particles was initially high, then decreased, and then increased, independent of particle size. In contrast, this trend was observed only for the 360 nm PS particles (Fig. 5). For mice administered the 230 nm PS particles, there was a higher percentage of cells initially associated with particles but decreased over the next 24 h while the opposite behavior was observed for the 2,200 nm PS particles with a significant increase in particle-positive cell population between 24 and 48 h. In addition, a statistically significant difference was observed between the groups of mice administered the larger

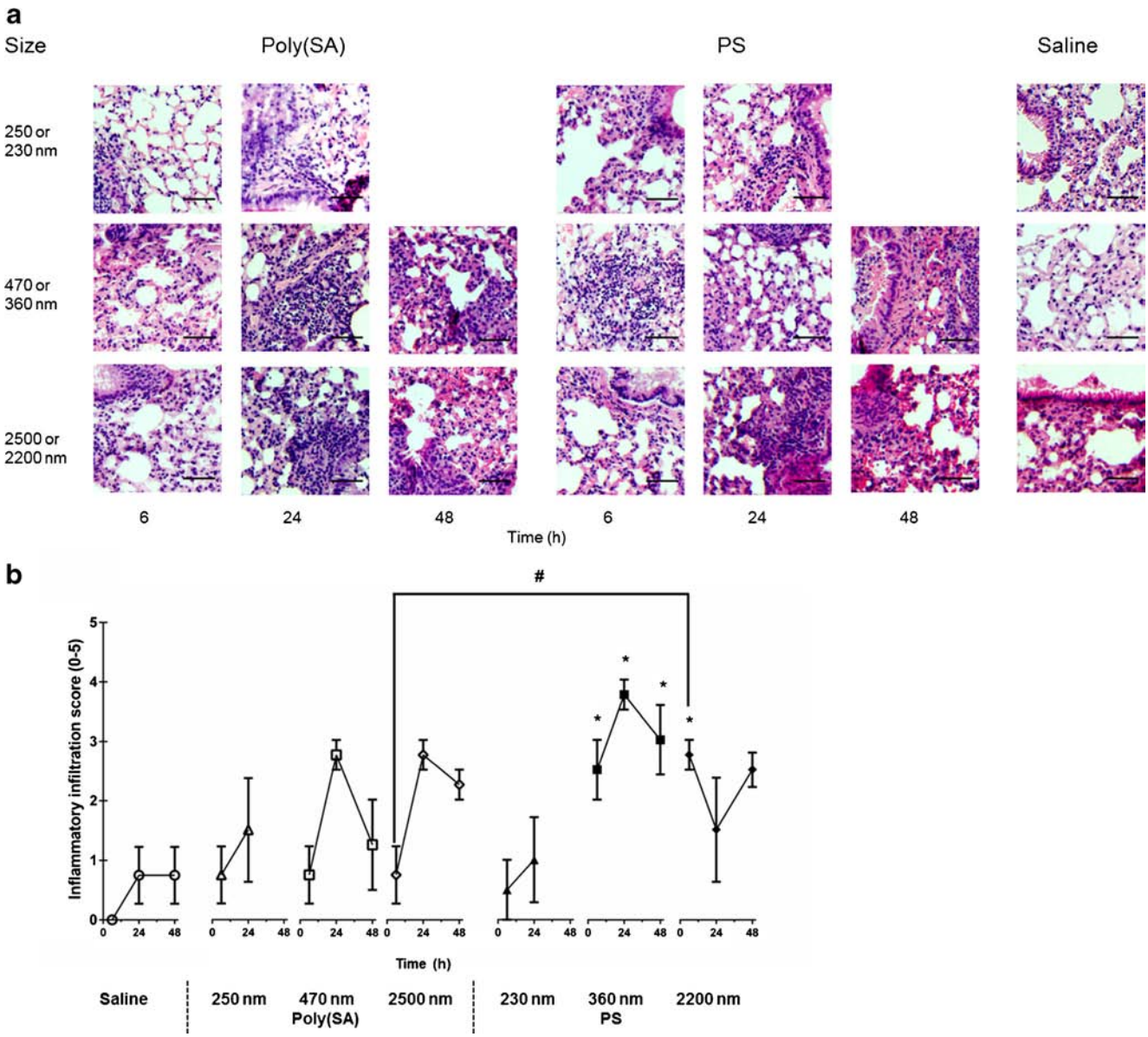

Fig. 4 Photomicrographs depicting histological changes of lung tissue after intranasal administration of nanoparticles. **a** All lung tissues were stained with H&E. Normal lung tissue images from three representative saline administered mice. Sample images were taken from one mouse for each particle size, chemistry and time combination. Scale bar on images is 50 um. **b** H&E stained lung tissues were evaluated, blindly, by a board-certified veterinary pathologist using a histopathological scoring system. Scores of 0–5 were assigned to five independent parameters. A score of 0 indicated the parameter was absent and a score of 5 indicated that the parameter was diffuse and interrupted normal tissue architecture. The data are presented as the mean ± standard error of the mean of the inflammatory infiltration score. The *asterisk* (*) indicates statistical significance compared to lungs from mice that were administered saline ($p < 0.05$). The *pound sign* (#) indicates significance between particle chemistries of a given size and specific time post-administration ($p < 0.05$). Each treatment group at each time point consisted of slides sectioned from a total of four mice. (magnification = 100X).

sized poly(SA) and PS particles in the percentage of cells positive for particles at 24 and 48 h post-administration. A greater percentage of cells were shown to be associated with the poly(SA) particles at 24 h and, as expected for non-degradable particles, there was a greater proportion of cell associated with the PS particles at 48 h. Overall, these findings are consistent with other independent studies in our group utilizing polydisperse antigen-loaded polyanhydride nanovaccines (33).

Characterization of cellular populations in lung tissue

The particle-positive cellular population (which is composed of dendritic cells (DCs), macrophages (MΦs), polymorphonuclear leukocytes (PMNs), and epithelial cells) was further characterized by flow cytometry using specific cell surface markers. Representative contour plots are depicted in Fig. 6. The viable particle-positive cell population was first gated into four distinct quadrants based on expression of the surface markers

Table II Total Number of Particle Positive Cells

Time [h]	Poly(SA) particle Diameter [nm]			PS particle Diameter [nm]		
	250	470	2,500	230	360	2,200
6	NS	3,119	1,554	2,500	1,825	NS
12	1,035	2,770	872	1,304	2,445	1,039
24	2,334	1,219	2,401	1,258	NS	NS
48	NA	2,716	1,604	NA	3,473	1,286

Total number of viable, single cells identified as particle positive with flow cytometry. Mean number of total events analyzed by flow cytometry was 92,000. Mean number of viable cells analyzed by flow cytometry was 63,000. The percentage of the viable population positive for particles is summarized in Figure 5.

CD11b, an integrin that serves as a MΦ marker (34,35), and CD11c, an integrin that differs in expression on DCs based upon cell origin (36). The four cell populations were further divided based on the level of expression of either Ly6 C/G, a marker for PMNs, or F4/80 (MΦ marker), which is negative on precursor cells, positive on mature MΦs ($F4/80^{high}$), but diminished on activated MΦs ($F4/80^{low}$) (37–39). Additionally, the cell surface molecule, CD324, a tight junction protein common to epithelial cells, was used to identify cells not expressing CD11b, CD11c, or Ly6 C/G (40). A representative example of the gating strategy with indications of cell surface marker-positive and -negative populations is shown in Fig. 6b.

The average percentage of particle-positive cells from mice administered a specific particle formulation (A–F) at the given time post-administration is shown as a pie chart in Fig. 7. Statistical analysis of the particle-positive cell populations is presented in Table III. Statistically significant differences in the phenotypes of the cells associated with particles were observed based on particle size, chemistry, and time after administration. At 6 h post-administration, there were similar percentages of the $CD11b^+/CD11c^+$ population (between 38 and 50%) that were particle-positive, with almost all of this population being $F4/80^+$ for the 230 nm PS particles (Fig. 7b). For the 360 nm PS particles, the $CD11b^+/CD11c^+$ population was dominant and significantly different than the other three CD11b/CD11c populations (i.e., $CD11b^+/CD11c^-$, $CD11b^-/CD11c^+$, and $CD11b^-/CD11c^-$) (Table III). The phenotypes of the cells that internalized the 470 nm poly(SA) particles were 40% $CD11b^+/CD11c^+$ and 60% $CD11b^+/CD11c^-$, significantly greater than the $CD11b^-/CD11c^+$ and $CD11b^-/CD11c^-$ populations (Table III). At 6 h post-administration, the only significant differences between the poly(SA) and the PS particle-positive cells were observed for the 470 nm poly(SA) and 360 nm PS particle groups. These differences occurred within the $CD11b^+/CD11c^-$/Ly6 C/G population, with the Ly6 C/G^- population being dominant for the poly(SA) particles at 49 *vs.* 0% of cells in the PS group (Fig. 7c and d, Table III). However, the 230 nm PS and 2,500 nm poly(SA) particles were associated with a significantly higher frequency of the $CD11b^+/CD11c^-$/Ly6 C/G^+ cell sub-population. At 6 h post-administration, there were no cells within the $CD11b^-/CD11c^+$ sub-population that were found to be positive for the 470 nm poly(SA) or the 360 nm PS particles (Fig. 7c and d, respectively). The $CD11b^-/CD11c^-$ sub-population is another dominant phenotype that exhibits the initial uptake of the 230 and 360 nm PS particles, with the 360 nm PS particles being almost exclusively in the Ly6 C/G^+ sub-population. The 230 nm PS particles were detected within all

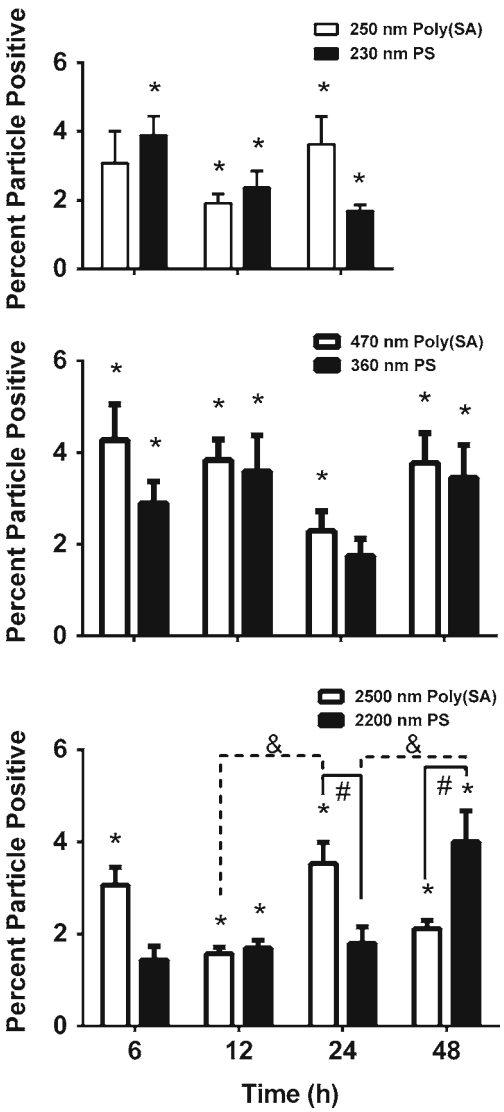

Fig. 5 Percentage of viable cells recovered from the lung homogenate that were positive for particles. The data are presented as the mean ± standard error of the mean. The *asterisk* (*) indicates significance compared to cells recovered form mice administered saline ($p < 0.05$). The *pound sign* (#) indicates significance between chemistries ($p < 0.05$). The *ampersand* (&) indicates significance between the indicated time points ($p < 0.05$). Each treatment group at each time point contained 10 mice.

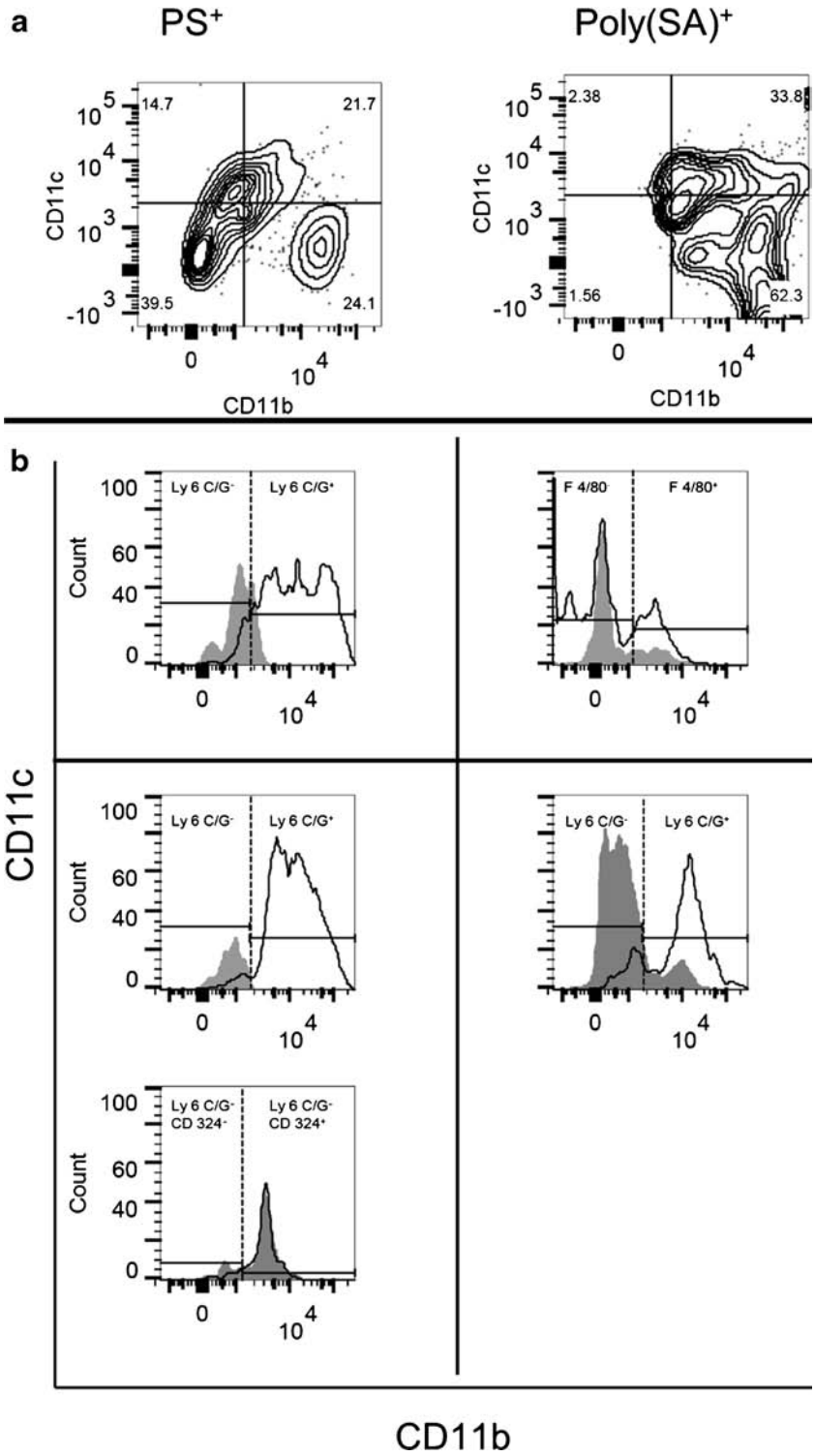

Fig. 6 Sample gating protocol used to identify particle positive cell types. **a** Contour plot of representative particle positive viable cell populations (12 h post-administration) separated into four quadrants based on CD11b and CD11c expression. **b** Each CD11b/CD11c quadrant was subsequently gated for either Ly6 C/G or F4/80 cell surface markers. The $CD11b^{-}$/$CD11c^{-}$/Ly6C/G^{-} sub-population was further analyzed with respect to CD324. Shaded histogram depicts the cells that internalized the 470 nm poly(SA) particles while open histogram represents the cells that took up the 360 nm PS particles. The vertical *dashed lines* indicate the delineation between positive and negative populations for the indicated marker.

the $CD11b^{-}$/$CD11c^{-}$ sub-populations (i.e., Ly6 C/G^{+}, Ly6 C/G^{-}/$CD324^{+}$, and Ly6 C/G^{-}/$CD324^{-}$).

Between 6 and 24 h post-administration, there was a significant increase in the percentage of the resident MΦ ($CD11b^{+}$/$CD11c^{+}$) population that were positive for the 230 nm PS particle-positive cells and contraction of all the other sub-populations except plasmacytoid DCs (pDCs, $CD11b^{-}$/$CD11c^{-}$/Ly6 C/G^{+}) which remained steady (Fig. 7b). At 12 h post-administration, the 250 nm poly(SA) and 230 nm PS particles were similarly associated with resident MΦs and $CD11b^{+}$/$CD11c^{-}$ populations, with fewer $CD11b^{-}$/$CD11c^{+}$ and $CD11b^{-}$/$CD11c^{-}$ cells associated

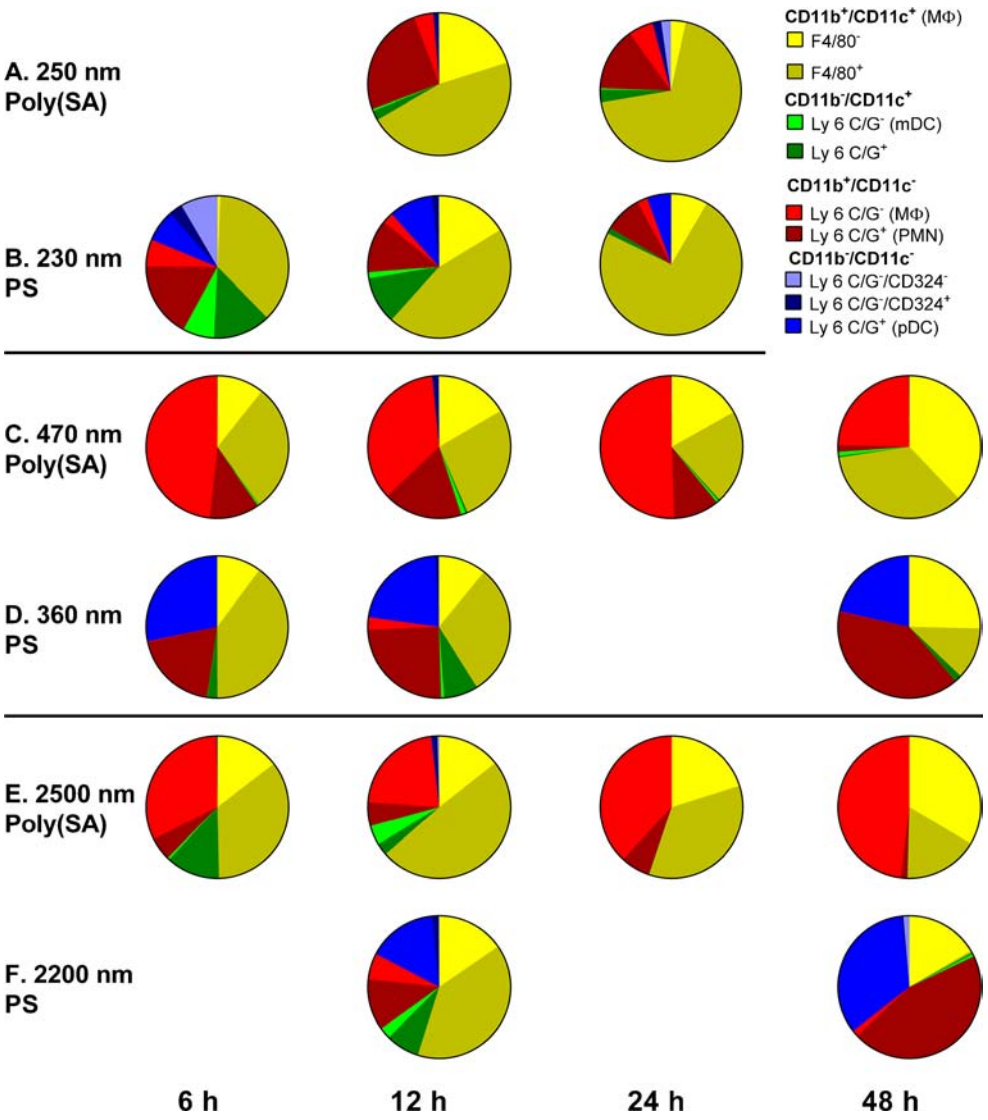

Fig. 7 Phenotypes of particle-positive cells from the lung tissue homogenate. Each pie chart shows the relative proportion of each cellular phenotype that was particle-positive for each chemistry and size of particle at different times post-administration. Each wedge of the pie chart represents different sub-populations of cells as shown in the legend ($n = 10$). Statistical evaluations are presented in Table III.

with the poly(SA) particles. However, between 12 and 24 h for both poly(SA) and PS particles, the percentage of particle-positive cells that were characterized as $F4/80^+$ resident MΦs significantly increased (Table III).

The 470 nm poly(SA) particles and the corresponding PS particles exhibited fewer changes in the cellular phenotype of cells positive for particles over the course of the study (Fig. 7c and d). The phenotype of cells positive for poly(SA) particles showed little change over the first 24 h and then showed significant expansion of both the $F4/80^-$ and $F4/80^+$ resident MΦ sub-populations and significant contraction of the $CD11b^+/CD11c^-$ population between 24 and 48 h (Table III). In contrast, in the lungs of mice administered the 360 nm PS particles there was a significant expansion of the PMN ($CD11b^+/CD11c^-$/Ly6 C/G^+) sub-population and significant contraction of $F4/80^+$ resident MΦ sub-population between 12 and 48 h (Table III). In comparing the 470 nm poly(SA) to the 360 nm PS particles, the $CD11b^+/CD11c^-$ population that was poly(SA) particle-positive was significantly greater than the corresponding PS particle-positive population at 6 and 12 h post-administration (Table III). By 48 h post-administration, there were more resident MΦs associated with the 470 nm poly(SA) particles and greater a percentage of PMNs associated with the 360 nm PS particles indicating a chemistry-mediated difference in the dynamics of the cellular populations associated with a given nanoparticle.

The larger-sized poly(SA) particles showed greater association with resident MΦ and $CD11b^+/CD11c^-$ cells than the other cell phenotypes (Fig. 7e). The 2,500 nm poly(SA) particle positive cells also displayed significant contraction of the $F4/80^+$ resident MΦ sub-population between 24 and 48 h,

Table III Type of Cell With Particles, Statistical Analysis of Cell Surface Marker Distributions

Cell Type	Time [h]	Poly(SA) Particle Diameter [nm]			PS Particle Diameter [nm]		
		250	470	2,500	230	360	2,200
Percent $CD11b^+$ $CD11c^+$	6		BCD,H	BD	FG	BCD	
	12	BCD	BD,H	BCD	BCD,EG	BD	BCD,H
	24	BCD	BCD,H	BD	BCD,EF		
	48		BCD,$,EFG	BD,$		B,$	CD,$,F
Percent $CD11b^+$ $CD11c^+$ $F4/80^{+,a}$	6			H	G	H	
	12	G		H	G	H	H
	24	F	H	H	EF		
	48		$,G	EFG		$,EF	F
Percent $CD11b^-$ $CD11c^+$	6		AC	AC		AD	
	12	AC	AC	AC	A	AC	A
	24		AC	AC			
	48		AC	AC		ACD	CD
Percent $CD11b^-$ $CD11c^+$ Ly6 $C/G^{+,a}$	6						
	12						
	24						
	48						
Percent $CD11b^+$ $CD11c^-$	6		ABD,$,H	BD		A,$,H	
	12	ABD	BD,$,H	ABD,GH	A	B,$	A,H
	24		ABD,H	BD,F			
	48		ABD,EFG	BD,F		BD,E	AB,F
Percent $CD11b^+$ $CD11c^-$ Ly6 $C/G^{+,a}$	6					H	
	12		H			H	H
	24						
	48		$,F	$		$,EF	$,F

Bold titles indicate parent CD11b/CD11c population

[a] Positive surface marker expression only included in table.

A - Significant difference between specified CD11b/CD11c population and $CD11b^+$ /$CD11c^+$ for given particle size and chemistry and at the specified time point ($p < 0.05$)

B - Significant difference between specified CD11b/CD11c population and $CD11b^-$ /$CD11c^+$ for given particle size and chemistry and at the specified time point ($p < 0.05$)

C - Significant difference between specified CD11b/CD11c population and $CD11b^+$ /$CD11c^-$ for given particle size and chemistry and at the specified time point ($p < 0.05$)

D - Significant difference between specified CD11b/CD11c population and $CD11b^-$ /$CD11c^-$ for given particle size and chemistry and at the specified time point ($p < 0.05$)

$ - Significant difference between poly(SA) and PS (both chemistries labeled) for given particle size, surface marker expression, and time point ($p < 0.05$)

E - Significantly different than 6 h time point for given particle size, chemistry, and surface marker expression ($p < 0.05$)

F - Significantly different than 12 h time point for given particle size, chemistry, and surface marker expression ($p < 0.05$)

G - Significantly different than 24 h time point for given particle size, chemistry, and surface marker expression ($p < 0.05$)

H - Significantly different than 48 h time point for given particle size, chemistry, and surface marker expression ($p < 0.05$)

and expansion of the $CD11b^+/CD11c^-$ population between 12 and 24 h. Comparing the 2,200 nm PS particle-positive cells between 12 and 48 h post-administration a significant contraction of the resident MΦs and expansion of the $CD11b^+/CD11c^-$ and $CD11b^-/CD11c^-$ populations were observed (Fig. 7f, Table III). Although no significant differences in particle positive cells based on chemistry were observed at 12 h between the larger-sized particles, the differing dynamics resulted in significant differences between chemistries at 48 h post-administration. These differences in particle-positive cells included a greater poly(SA)-positive resident MΦ population, and greater PS-positive $CD11b^-/$

$CD11c^-$ population and pDC and PMN sub-populations (Fig. 7e and f, Table III).

DISCUSSION

The studies described herein were designed to evaluate the role of primary particle size and polymer chemistry on the efficiency of respiratory deposition of intranasally administered nanoparticles to mice and the phenotype of cells associated with particles. Overall, this work demonstrated that particle size and chemistry can be exploited to tune the pulmonary deposition and biodistribution within specific populations of phagocytes in the respiratory tract of mice.

To evaluate the effect of particle chemistry, care was taken to match the morphology and primary particle size distributions of the biodegradable poly(SA) and the non-degradable PS particles. The synthesized monodisperse poly(SA) particles as well as the commercially purchased PS particles exhibited smooth and spherical morphology (Fig. 1a). Based on the morphological and particle size uniformity (Fig. 1b and c) as well as statistical analysis of the particle size distributions (Table I), the poly(SA) particle size was considered to be directly comparable to the corresponding PS particle size.

The data presented herein show that primary particle size is an important determinant of effective deposition into the lungs. This is consistent with previous work in which nebulized submicron particles were deposited within the lungs, while nebulized 1,600 nm particles failed to be detected in the lung (16). In this work, the data demonstrated that the 470 nm poly(SA) and the 360 nm PS particles were effectively deposited in the lungs at 6 h post-administration (Figs. 2 and 3). This suggests that, independent of particle chemistry, a critical size range (360 to 470 nm) may exist that allows for maximum respiratory deposition from a single dose of intranasally administered particles. The punctate fluorescent signal suggests the aggregation of particles within the lung (Fig. 2). The pattern of particle localization observed could be due to the method of administration (e.g., droplet *vs.* nebulized) or associated with anatomical features/restrictions within the lungs.

The decrease in the MFI of the poly(SA) particles is consistent with the erosion characteristics of this chemistry and/or the removal of poly(SA) particles from the lungs by phagocytic cells. While there is a clear range of particle size for maximum respiratory deposition, the inability to detect the smaller or larger poly(SA) particles at 6 h (Fig. 3) can be attributed to the sensitivity of the detection method, as there were significant populations of lung homogenate cells containing poly(SA) particles of all sizes studied (Fig. 5).

An important consideration in this analysis is that once the particles are deposited in the lung, there are multiple host mechanisms that can redistribute or clear the particles from the lung (41–44). In the conducting airways, mucus will entrap particles which will be transported by mucocilliary and cough clearance from the lung or swallowed (42). Particles that deposit in the respiratory tract will be taken up by resident alveolar MΦs, other phagocytic cells (e.g., PMNs), and the respiratory epithelium (43). Based on the work of Blank and co-workers, these phagocytic cells (dendritic cells identified specifically as $CD11c^+$/MHC II^+ but both CD11b high and low) were observed to transport internalized particles out of the lung and to the draining lymph node and the rate of this transport was influenced by the particle size (45). There are many types of cells resident in the respiratory tract that influence the biological response to inhaled particles, including various types of epithelial cells, DCs, and MΦs (46). A more comprehensive panel of monoclonal antibodies to characterize the cell surface marker expression of cells within a total lung homogenate has been suggested by Misharin *et al.* (47). Definitive determination of cell types is difficult to achieve in the lung due to overlapping expression of surface markers between populations, recruitment of cells, and modulation of specific surface marker expression due to cellular maturity or activation (37–39,45,46,48–54). For example, the myeloid DCs (mDC, $CD11b^-/CD11c^+$/Ly6 C/G^-) sub-population can include T cells, DCs, alveolar MΦs, and/or non-migratory MΦs (45,49,53). Based on the histological evaluations, we observed a more pronounced inflammatory response in the tissue of mice administered the PS particles than in the lung tissue of the mice administered poly(SA) particles. Based on these initial host responses, which are a strong function of particle size and surface properties, chemokines are likely differentially produced that will recruit cells into interstitial pulmonary tissues and the airspaces where they aid in the uptake and removal of this particulate material. Although not specifically tested in this work, this would suggest differences in cell signaling based on the different polymer chemistries that could influence the downstream immune response induced.

After deposition, the cell-particle interactions were influenced by both particle size and chemistry. For the mice treated with smaller particles 250 nm poly(SA) and the 230 nm PS, the infiltration of inflammatory cells into the respiratory spaces were minimal and not significantly different than saline administered mice (Fig. 4). For the smallest size investigated (i.e., 250 nm poly(SA) and 230 nm PS), mice administrated poly(SA) and PS particles showed similar percentages of particle-positive cells with correspondingly similar particle-positive cellular phenotypes (Figs. 3, 5, 7a and b). Particles of this size also associated with the widest breadth of cell types within the first 6 h across all CD11b/CD11c populations (Fig. 7c–f). Despite the wide distribution of cell types, the majority of cells containing particles were APC phenotypes (resident MΦs, mDCs, and recruited MΦs ($CD11b^+/CD11c^-$/Ly6 C/G^-)) (Fig. 7a and b, Table III). The majority of the cells positive for the 230 nm PS or 250 nm poly(SA) particles were $CD11c^+$, which is consistent with the

particle-positive cell sub-population identified by Blank and co-workers for PS particles with sizes ranging from 20 to 1,000 nm (45). Blank *et al.* also showed that the migration of particle positive DCs from the lung to the draining lymph node was dependent upon particle size, with the DCs containing the smaller particles (i.e., 20 and 50 nm) arriving in the lymph node more rapidly. By 24 h post-administration, both the 250 nm poly(SA) and the 230 nm PS particles predominately associated with the $F4/80^+$ population (e.g., resident MΦ) (Fig. 7a and b). The reduction of other APC phenotypes positive for particles by 24 h suggests that either we are observing the migration of cells with internalized particles out of the lung or kinetic changes in the surface marker expression of particle positive cells.

Particle chemistry differences were more pronounced at the larger particle sizes. There was greater amount of inflammatory infiltration in the lungs of mice administered PS than poly(SA) particles (Fig. 4). However, a greater percentage of the lung cellular population was positive for the 470 nm poly(SA) particles compared to the 360 nm PS particles. Additionally, a significant difference was observed in cellular association between the larger-sized poly(SA) and PS particles, especially at 24 h or later (Fig. 5). These findings suggests that more cells present in the respiratory tract associate with 470 nm poly(SA) particles than the 360 nm PS particles.

In this work, fewer particle-positive PMNs were detected after administration of the 470 nm and 2,500 nm poly(SA) particles than the equivalent sized PS particles over the entire duration of the study (Table III, Fig. 7c–f). The granulocyte population within the lung has been associated with pulmonary inflammatory responses (48,49,55,56). Likewise, fewer poly(SA) particles associated with pDCs than PS particles. The data depicted in Figs. 5 and 7 supports this observation. A representative example of this cell marker for cells associated with the 470 nm poly(SA) and the 360 nm PS particles clearly demonstrates these differences (Fig. 6). The limited association of poly(SA) particles with granulocytes (in comparison to PS particles, as shown in Table III and Fig. 7d and f) is consistent with previous work from our laboratories that demonstrated the mild inflammatory response induced by polyanhydride nanovaccines upon intranasal administration (33). This is further supported by the differences in inflammatory infiltrate into the respiratory system after administration, with PS being significantly greater than saline administered mice (Fig. 4). This is also consistent with the observation that the type of cell infiltrate in the PS administered mice contained more PMNs as opposed to a MΦ and PMN mix that was observed for poly(SA). In this work, particle association with cells expressing the mDC cell surface phenotype was only observed for the 230 nm PS particles at 6 h (Fig. 7b). This suggests that internalization kinetics by this population of phagocytes is dependent upon both particle size and chemistry. The rapid disappearance of this cell population by 12–24 h is consistent with previous observations indicating that cells expressing these surface markers migrate out of the lungs to the draining lymph node (57). This clearly has implications for this cell type to be instrumental in the induction of an immune response. The findings from this work suggest that multiple sizes of erodible particles may facilitate the maintenance of an antigenic depot to effectively deliver antigen to the draining lymph node.

Particle chemistry influenced particle association with the recruited MΦ sub-population, with a greater percentage of cells associating with the 470 nm and 2,500 nm poly(SA) particles in comparison to PS particle-positive cells (Fig. 7d–f). A previous study also identified this sub-population of cells as $CD4^-$ and $CD8^-$ MΦs (49). In that study, significant increases in both the MΦ and neutrophil ($CD11b^+$, $CD11c^-$, Ly6 C/G^+, $CD4^-$, and $CD8^-$) populations were observed in whole lung homogenate 2 days after infection with highly pathogenic influenza virus, suggesting a net influx of these populations into the lung after infection. In the current work, we observed both a MΦ and neutrophil infiltration in the majority of poly(SA) administered mice while the infiltration for PS administered mice was predominantly neutrophils. The only qualitative difference in the MΦ population associated with the poly(SA) particles in this work was a slight reduction by 48 h for the 470 nm size (Fig. 7c).

The current work suggests several different factors for the clearance of particles from the lung based on size and chemistry. Initially, the primary size of the particles (and not the chemistry) is the dominant factor that determines the amount of deposition in the respiratory tract as demonstrated by the enhanced deposition of the intermediate (i.e., 360–470 nm) size particles. However, with time, a combination of particle size and chemistry influenced the recruitment of innate immune cells into the lung and degree to which cells associated with the particles. As the size of the biodegradable poly(SA) particles is reduced over time because of erosion (58) and as the particles are internalized by phagocytic cells, the dynamics of clearance from the lung and cellular association were modulated. More poly(SA) particles associated with phagocytic cells than did PS particles. Based on our previous *in vitro* work (59), this observation suggests that the internalization of poly(SA) particles would induce the secretion of cytokines and chemokines. Additional factors that may affect the dynamics of particle clearance include the adsorption of proteins onto the surface of the particles, mucocilliary clearance of particles entrapped in mucus, migration of phagocytic cells with particles from the respiratory to the lymphatic system, and non-cell mediated removal of particles from the respiratory tract.

CONCLUSIONS

By using monodisperse particles, this work provides new insights about the pulmonary biodistribution and cellular

association of nanoparticles with respect to particle size and chemistry. Herein, it was demonstrated that the initial deposition of intranasally administered particles in suspension is dependent on primary particle size, with maximal deposition demonstrated for the 360–470 nm particles, regardless of chemistry. The type of innate immune cell recruited and extent of infiltration into the lung was dependent on both particle size and chemistry. With time, both particle size and chemistry affected the specific types of cells that associated with particles, and therefore the dynamics of particle clearance from the lung. The current studies provide important underpinnings that enhance our understanding of the impact that delivery vehicle design has upon biodistribution and cellular association in the respiratory system. These insights are valuable for the rational design of pulmonary vehicles for vaccine delivery.

ACKNOWLEDGMENTS

The authors wish to acknowledge funding from the ONR-MURI Award (NN00014-06-1-1176), the U.S. Army Medical Research and Materiel Command (Grant no. W81XWH-09-1-0386), and HRSA (Grant no. C76HF19578). The authors would also like to thank Shawn Rigby of the Iowa State Flow Cytometry Facility for his expertise in flow cytometry. BN acknowledges the Vlasta Klima Balloun Professorship in Chemical and Biological Engineering. The authors wish to thank Dr. Paola Boggiatto for useful discussions on the analysis of the flow cytometric data.

REFERENCES

1. Buxton DB. Nanotechnology in the diagnosis and management of heart, lung and blood diseases. Expert Rev Mol Diagn. 2007;7:149–60.
2. Kumari A, Yadav SK, Yadav SC. Biodegradable polymeric nanoparticles based drug delivery systems. Colloids Surf B. 2010;75(1):1–18.
3. McNeela EA, Lavelle EC. Recent advances in microparticle and nanoparticle delivery vehicles for mucosal vaccination. Curr Top Microbiol Immunol. 2012;354:75–99.
4. Park E-S, Maniar M, Shah JC. Biodegradable polyanhydride devices of cefazolin sodium, bupivacaine, and taxol for local drug delivery: preparation, and kinetics and mechanism of *in vitro* release. J Control Release. 1998;52(1–2):179–89.
5. Storm PB, Moriarity JL, Tyler B, Burger PC, Brem H, Weingart J. Polymer delivery of camptothecin against 9L gliosarcoma: release, distribution, and efficacy. J Neuro-Oncol. 2002;56:209–17.
6. Masters DB, Berde CB, Dutta S, Turek T, Langer R. Sustained local anesthetic release from bioerodible polymer matrices: a potential method for prolonged regional anesthesia. Pharm Res. 1993;10(10):1527–32.
7. Carino GP, Jacob JS, Mathiowitz E. Nanosphere based oral insulin delivery. J Control Release. 2000;65(1–2):261–9.
8. Erdmann L, Uhrich KE. Synthesis and degradation characteristics of salicylic acid-derived poly(anhydride-esters). Biomaterials. 2000;21:1941–6.
9. Deng J-S, Meisters M, Li L, Setesak J, Claycomb L, Tian Y, *et al.* The development of an injection-molding process for a polyanhydride implant containing gentamicin sulfate. PDA J Pharm Sci Technol. 2002;56(2):65–77.
10. Weiner AA, Bock EA, Gipson ME, Shastri VP. Photocrosslinked anhydride systems for long-term protein release. Biomaterials. 2008;29(15):2400–7.
11. Fv B, Schedl L, Göpferich A. Why degradable polymers undergo surface erosion or bulk erosion. Biomaterials. 2002;23(21):4221–31.
12. Balasse E, Odot J, Gatouillat G, Andry M-C, Madoulet C. Enhanced Immune response induced by bsa loaded in hydroxyethylstarch microparticles. Int J Pharm. 2008;353(1–2):131–8.
13. Huntimer L, Ramer-Tait AE, Petersen LK, Ross KA, Walz KA, Wang C, *et al.* Evaluation of biocompatiblity and administration site reactogenicity of polyanhydride-particle-based platform for vaccine delivery. Adv Healthc Mater. 2013;2:369–78.
14. Kuehl PJ, Anderson TL, Candelaria G, Gershman B, Harlin K, Hesterman JY, *et al.* Regional particle size dependent deposition of inhaled aerosols in rats and mice. Inhal Toxicol. 2012;24(1):27–35.
15. Champion JA, Walker A, Mitragotri S. Role of particle size in phagocytosis of polymeric microspheres. Pharm Res. 2008;25(8):1815–21.
16. Chiang P-C, Alsup J, Lai Y, Hu Y, Heyde B, Tung D. Evaluation of aerosol delivery of nanosuspension for Pre-clinical pulmonary drug delivery. Nanoscale Res Lett. 2009;4(3):254–61.
17. Wang SH, Thompson AL, Hickey AJ, Staats HF. Dry powder vaccines for mucosal administration: critical factors in manufacture and delivery. Curr Top Microbiol Immunol. 2012;354:121–56.
18. Wilson-Welder JH, Torres MP, Kipper MJ, Mallapragada SK, Wannemuehler MJ, Narasimhan B. Vaccine adjuvants: current challenges and future approaches. J Pharm Sci. 2009;98(4):1278–316.
19. Ulery BD, Phanse Y, Sinha A, Wannemuehler MJ, Narasimhan B, Bellaire BH. Polymer chemistry influences monocytic uptake of polyanhydride nanospheres. Pharm Res. 2009;26(3):683–90.
20. Champion JA, Mitragotri S. Shape induced inhibition of phagocytosis of polymer particles. Pharm Res. 2009;26(1):244–9.
21. Petersen LK, Xue L, Wannemuehler MJ, Rajan K, Narasimhan B. The simultaneous effect of polymer chemistry and device geometry on the in vitro activation of murine dendritic cells. Biomaterials. 2009;30(28):5131–42.
22. Ulery BD, Petersen LK, Phanse Y, Kong CS, Broderick SR, Kumar D, *et al.* Rational design of pathogen-mimicking amphiphilic materials as nanoadjuvants. Sci Rep. 2011;1:1–9.
23. Ulery BD, Kumar D, Ramer-Tait AE, Metzger DW, Wannemuehler MJ, Narasimhan B. Design of a protective single-dose intranasal nanoparticle-based vaccine platform for respiratory infectious diseases. PLoS One. 2011;6(3):e17642.
24. Jani PU, Florence AT, McCarthy DE. Further histological evidence of the gastrointestinal absorption of polystyrene nanospheres in the Rat. Int J Pharm. 1992;84:245–52.
25. Brooking J, Davis SS, Illum L. Transport of nanoparticles across the rat nasal mucosa. J Drug Target. 2001;9:267–79.
26. Kipper MJ, Shen E, Determan A, Narasimhan B. Design of an injectable system based on bioerodible polyanhydride microspheres for sustained drug delivery. Biomaterials. 2002;23(22):4405–12.
27. Shen E, Kipper MJ, Dziadul B, Lim M-K, Narasimhan B. Mechanistic relationships between polymer microstructure and drug release kinetics in bioerodible polyanhydrides. J Control Release. 2002;82(1):115–25.
28. Roberts JR, Antonini JM, Porter DW, Chapman RS, Scabilloni JF, Young S-H, *et al.* Lung toxicity and biodistribution of Cd/Se-ZnS quantum dots with different surface functional groups after pulmonary exposure in rats. Part Fibre Toxicol. 2013;10(5).
29. Determan AS, Trewyn BG, Lin VSY, Nilsen-Hamilton M, Narasimhan B. Encapsulation, stabilization, and release of BSA-FITC from polyanhydride microspheres. J Control Release. 2004;100(1):97–109.

30. Determan AS, Wilson JH, Kipper MJ, Wannemuehler MJ, Narasimhan B. Protein stability in the presence of polymer degradation products: consequences for controlled release formulations. Biomaterials. 2006;27(17):3312–20.
31. Determan AS, Graham JR, Pfeiffer KA, Narasimhan B. The role of microsphere fabrication methods on the stability and release kinetics of ovalbumin encapsulated in polyanhydride microspheres. J Microencapsul. 2006;23(8):832–43.
32. Torres MP, Vogel BM, Narasimhan B, Mallapragada SK. Synthesis and characterization of novel polyanhydrides with tailored erosion mechanisms. J Biomed Mater Res Part A. 2006;76A(1):102–10.
33. Ross KA, Haughney SL, Petersen LK, Boggiatto P, Wannemuehler MJ, Narasimhan B. Lung deposition and cellular uptake behavior of pathogen-mimicking nanovaccines in the first 48 hours. Adv Health Mater. 2014;3(7):1071–7.
34. Springer T, Galfré G, Secher DS, Milstein C. Mac-1: a macrophage differentiation antigen identified by monoclonal antibody. Eur J Immunol. 1979;9(4):301–6.
35. Springer TA, Dav:Gnon D, Ho M-K, Kurzinger K, Martz E, Sanchez-Madrid F. LFA-1 and Lyt-2,3, molecules associated with T lymphocyte-mediated killing; and Mac-1, an LFA-1 homologue associated with complement receptor Function1. Immunol Rev. 1982;68(1):171–96.
36. Metlay JP, Witmer-Pack MD, Agger R, Crowley MT, Lawless D, Steinman RM. The distinct leukocyte integrins of mouse spleen dendritic cells as identified with New hamster monoclonal antibodies. J Exp Med. 1990;171(5):1753–71.
37. Hirsch S, Gordon S. The Use and limitation of monoclonal antibodies against mononuclear phagocytes. Immunobiology. 1982;161:298–307.
38. Vermaelen K, Pauwels R. Accurate and simple discrimination of mouse pulmonary dendritic cell and macrophage populations by flow cytometry: methodology and new: insights. Cytom Part A. 2004;61A:170–7.
39. Matthews KE, Karabeg A, Roberts JM, Saeland S, Dekan G, Epstein MM, *et al.* Long-term deposition of inhaled antigen in lung resident CD11b-CD11c+ cells. Am J Respir Cell Mol Biol. 2007;36:435–41.
40. Marsh LM, Cakarova L, Kwapiszewska G, von Wulffen W, Herold S, Seeger W, *et al.* Surface expression of CD74 by type II alveolar epithelial cells: a potential mechanism for macrophage migration inhibitory factor-induced epithelial repair. Am J Physiol Lung Cell Mol Physiol. 2009;296(3):L442–52.
41. Patton JS, Brain JD, Davies LA, Fiegel J, Gumbleton M, Kim K-J, *et al.* The particle has landed - characterizing the fate of inhaled pharmaceuticals. J Aerosol Med Pulm Drug Deliv. 2010;23(S2):S-71–87.
42. Kirch J, Guenther M, Doshi N, Schaefer UF, Schneider M, Mitragotri S, *et al.* Mucociliary clearance of micro- and nanoparticles is independent of size, shape and charge—an ex vivo and in silico approach. J Control Release. 2012;159(1):128–34.
43. Blank F, Stumbles P, von Garnier C. Opportunities and challenges of the pulmonary route for vaccination. Expert Opin Drug Deliv. 2011;8(5):547–63.
44. Geiser M, Kreyling WG. Deposition and biokinetics of inhaled nanoparticles. Part Fibre Toxicol. 2010;7(2).
45. Blank F, Stumbles PA, Seydoux E, Holt PG, Fink A, Rothen-Rutishauser B, *et al.* Size-dependent uptake of particles by pulmonary APC populations and trafficking to regional lymph nodes. Am J Respir Cell Mol Biol. 2013;49(1):67–77.
46. von Garnier C, Filgueira L, Wikstrom M, Smith M, Thomas JA, Strickland DH, *et al.* Anatomical location determines the distribution and function of dendritic cells and other APCs in the respiratory tract. J Immunol. 2005;175(3):1609–18.
47. Misharin AV, Morales-Nebreda L, Mutlu GM, Budinger GRS, Perlman H. Flow cytometric analysis of the macrophages and dendritic cell subsets in the mouse lung. Am J Respir Cell Mol Biol. 2013;49:503–10.
48. Gonzalez-Juarrero M, Shim TS, Kipnis A, Junqueira-Kipnis AP, Orme IM. Dynamics of macrophage cell populations during murine pulmonary tuberculosis. J Immunol. 2003;171:3128–35.
49. Perrone LA, Plowden JK, García-Sastre A, Katz JM, Tumpey TM. H5N1 and 1918 pandemic influenza virus infection results in early and excessive infiltration of macrophages and neutrophils in the lungs of mice. PLoS Pathog. 2008;4(8):e1000115.
50. Nakano H, Yanagita M, Gunn MD. Cd11c+B220+Gr-1+ cells in mouse lymph nodes and spleen display characteristics of plasmacytoid dendritic cells. J Exp Med. 2001;194(8):1171–8.
51. Jakubzick C, Tacke F, Llodra J, van Rooijen N, Randolph GJ. Modulation of dendritic cell trafficking to and from the airways. J Immunol. 2006;176(6):3578–84.
52. Janssen WJ, Barthel L, Muldrow A, Oberley-Deegan RE, Kearns MT, Jakubzick C, *et al.* Fas determines differential fates of resident and recruited macrophages during resolution of acute lung injury. Am J Respir Crit Care Med. 2011;184:547–60.
53. Lambrecht BN, Hammad H. Lung dendritic cells in respiratory viral infection and asthma: from protection to immunopathology. Annu Rev Immunol. 2012;30:243–70.
54. Langlois RA, Legge KL. Plasmacytoid dendritic cells enhance mortality during lethal influenza infections by eliminating virus-specific CD8 T cells. J Immunol. 2010;184:4440–6.
55. Julia V, Hessel EM, Malherbe L, Glaichenhaus N, O'Garra A, Coffman RL. A restricted subset of dendritic cells captures airborne antigens and remains able to activate specific T cells long after antigen exposure. Immunity. 2002;16:271–83.
56. Rose CE, Lannigan JA, Kim P, Lee JJ, Fu SM, Sung SS. Murine lung eosinophil activation and chemokine production in allergic airway inflammation. Cell Mol Immunol. 2010;7(5):361–74.
57. Bosio CM, Goodyear AW, Dow SW. Early interaction of *Yersinia pestis* with APCs in the lung. J Immunol. 2005;175:6750–6.
58. Sackett CK, Narasimhan B. Mathematical modeling of polymer erosion: consequences for drug delivery. Int J Pharm. 2011;418:104–14.
59. Chavez-Santoscoy AV, Roychoudhury R, Pohl NLB, Wannemuehler MJ, Narasimhan B, Ramer-Tait AE. Tailoring the immune response by targeting C-type lectin receptors on alveolar macrophages using "pathogen-like" amphiphilic polyanhydride nanoparticles. Biomaterials. 2012;33:4762–72.